

Production of Inert Scalars at the high energy e^+e^- colliders

Majid Hashemi,^a Maria Krawczyk,^b Saereh Najjari,^b Aleksander Filip Żarnecki^b

^a*Physics Department, College of Sciences,
Shiraz University, Shiraz, 71946-84795, Iran*

^b*Faculty of Physics, University of Warsaw,
Pasteura 5, 02-093 Warsaw, Poland*

E-mail: hashemi_mj@shirazu.ac.ir, maria.krawczyk@fuw.edu.pl,
saereh.najjari@fuw.edu.pl, zarnecki@fuw.edu.pl

ABSTRACT: We investigate the phenomenology of the light charged and neutral scalars in Inert Doublet Model at future e^+e^- colliders with center of mass energies of 0.5 and 1 TeV, and integrated luminosity of 500 fb^{-1} . The analysis covers two production processes, $e^+e^- \rightarrow H^+H^-$ and $e^+e^- \rightarrow AH$, and consists of signal selections, cross section determinations as well as dark matter mass measurements. Several benchmark points are studied with focus on $H^\pm \rightarrow W^\pm H$ and $A \rightarrow ZH$ decays. It is concluded that the signal will be well observable in different final states allowing for mass determination of all new scalars with statistical precision of the order of few hundred MeV.

KEYWORDS: Beyond Standard Model, Inert Doublet Model, Inert Scalars, Dark Matter, e^+e^- Colliders

Contents

1	Introduction	1
2	Inert Doublet Model	2
3	Software Setup	4
4	$e^+e^- \rightarrow H^+H^-$	5
4.1	Signal and Background Cross Sections	5
4.2	Event Generation and Analysis	6
4.2.1	Semi-leptonic Final State	7
4.2.2	Fully Hadronic Final State	10
5	$e^+e^- \rightarrow AH$	14
5.1	Signal and Background Cross Sections	14
5.1.1	Leptonic Final State	15
5.1.2	Hadronic Final State	17
6	Dark Matter Mass Measurement	19
7	Conclusions	22

1 Introduction

Inert Doublet Model (IDM) is one of the simplest extensions of the Standard Model (SM), with an additional $SU(2)$ scalar doublet, which can provide a dark matter candidate [1–8]. The scalar sector of IDM consist of two $SU(2)$ doublets where one is the SM-like Higgs doublet while the other is the inert or dark doublet. The scalar sector of the theory respects a discrete Z_2 symmetry under which the SM Higgs doublet Φ_S is *even* (as well as all the other SM fields) while the inert doublet Φ_D is *odd*, i.e. $\Phi_S \rightarrow \Phi_S$ (SM \rightarrow SM) and $\Phi_D \rightarrow -\Phi_D$. Due to the Z_2 symmetry, only the SM Higgs doublet acquires a non-zero vacuum expectation value and hence is a source of electroweak symmetry breaking (EWSB). After EWSB in the scalar sector this model has five physical states: the SM Higgs boson h as well as two charged scalars, H^\pm , and two neutral ones, H and A . Since the inert doublet is odd under Z_2 symmetry, the lightest inert particle is a natural candidate for dark matter. Also due to the Z_2 symmetry, the inert doublet does not couple with the fermions of the SM through Yukawa-type interactions. This model provides description of the evolution

of the universe [9] and strong first order phase transition, needed for baryogenesis [10–13].

In this work, we consider scenarios where H boson is the dark matter candidate ($m_H < m_{H^\pm}, m_A$), using the benchmark points suggested in Ref. [14], which satisfy all the recent experimental and theoretical constraints. We study the potential of the future e^+e^- colliders, like ILC or CLIC, for testing the IDM; other analyses of the IDM at colliders were done in [8, 15–24]. We focus on the charged scalar ($H^+ H^-$) production and the neutral scalar ($H A$) production at the center of mass energies of 0.5 TeV and 1 TeV, with the integrated luminosity of 500 fb^{-1} corresponding to the first 4 years of ILC running [25]. In particular we consider the following decay processes:

$$\begin{aligned} e^+e^- &\rightarrow H^+H^- \rightarrow W^+W^-HH \rightarrow \ell\nu jjHH, jjjjHH, \\ e^+e^- &\rightarrow HA \rightarrow HHZ \rightarrow HH\ell\ell, HHjj. \end{aligned} \quad (1.1)$$

A similar analysis for different benchmark points at the ILC with center of mass energies of 250 GeV to 500 GeV has been performed in [15]. The analysis of the Compressed IDM (with a degenerated spectrum of inert scalars) have been recently studied in [26] for LEP, as well as for LHC and ILC.

The paper is organized as follows. Essential details of our model setup and the benchmark points are described in section 2. In section 3 we provide the description of simulation tools used in the analysis. Sections 4 and 5 contain the details of the event generation and physics analysis of our benchmark points for $e^+e^- \rightarrow H^+H^-$ and $e^+e^- \rightarrow AH$, respectively. In section 6 we propose a procedure for the measurement of the dark matter mass. Finally, the conclusions are given in section 7.

2 Inert Doublet Model

The scalar sector of IDM consists of two scalar doublets, the SM Higgs doublet Φ_S with SM-like Higgs boson h and the inert doublet Φ_D . Only the SM Higgs doublet (Φ_S) interacts with the SM fermions, whereas the inert doublet (Φ_D) is Z_2 odd and it does not interact with the SM fermions through Yukawa-type interactions. The two doublets can be parameterised as follows,

$$\Phi_S = \begin{pmatrix} G^\pm \\ \frac{v+h+iG^0}{\sqrt{2}} \end{pmatrix}, \quad \Phi_D = \begin{pmatrix} H^\pm \\ \frac{H+iA}{\sqrt{2}} \end{pmatrix}, \quad (2.1)$$

with the vacuum expectation value $v = 246 \text{ GeV}$ (the SM value). The most general scalar potential for the IDM has the following form:

$$\begin{aligned} V(\Phi_S, \Phi_D) = & -\frac{1}{2} \left[m_{11}^2 (\Phi_S^\dagger \Phi_S) + m_{22}^2 (\Phi_D^\dagger \Phi_D) \right] + \frac{\lambda_1}{2} (\Phi_S^\dagger \Phi_S)^2 + \frac{\lambda_2}{2} (\Phi_D^\dagger \Phi_D)^2 \\ & + \lambda_3 (\Phi_S^\dagger \Phi_S) (\Phi_D^\dagger \Phi_D) + \lambda_4 (\Phi_S^\dagger \Phi_D) (\Phi_D^\dagger \Phi_S) + \frac{\lambda_5}{2} \left[(\Phi_S^\dagger \Phi_D)^2 + (\Phi_D^\dagger \Phi_S)^2 \right]. \end{aligned} \quad (2.2)$$

The above potential has seven parameters $(m_{11,22}, \lambda_{1,2,3,4,5})$ that we assume to be real. The scalar masses are as follows:

$$\begin{aligned} m_h^2 &= \lambda_1 v^2 = m_{11}^2, \\ m_{H^\pm}^2 &= \frac{1}{2}(\lambda_3 v^2 - m_{22}^2), \\ m_H^2 &= \frac{1}{2}(\lambda_{345} v^2 - m_{22}^2), \\ m_A^2 &= \frac{1}{2}(\bar{\lambda}_{345} v^2 - m_{22}^2), \end{aligned} \tag{2.3}$$

with $\lambda_{345} \equiv \lambda_3 + \lambda_4 + \lambda_5$ and $\bar{\lambda}_{345} \equiv \lambda_3 + \lambda_4 - \lambda_5$.

Theoretical Constraints

The scalar potential $V(\Phi_S, \Phi_D)$ (2.2) has to satisfy many theoretical and experimental constraints, as discussed in Ref. [14], which we have to take into account when defining benchmark scenarios. The vacuum stability at tree level leads to the following conditions on the couplings:

$$\lambda_1 \geq 0, \lambda_2 \geq 0, \sqrt{\lambda_1 \lambda_2} + \lambda_3 > 0, \sqrt{\lambda_1 \lambda_2} + \lambda_{345} > 0 \tag{2.4}$$

To have the inert vacuum as a global minimum of the potential, we require [27]¹:

$$\frac{m_{11}^2}{\sqrt{\lambda_1}} \geq \frac{m_{22}^2}{\sqrt{\lambda_2}}. \tag{2.5}$$

We also require perturbative unitarity of $2 \rightarrow 2$ scalar scattering matrix.

Experimental Constraints

We set the mass of the SM-like Higgs boson h to be $M_h = 125$ GeV [30] and impose the upper bound on the total width of h , $\Gamma_{tot} \leq 22$ MeV [31, 32]. Total widths of W and Z boson imply the following bounds [33]:

$$m_H + m_A \geq m_Z, \quad 2m_{H^\pm} \geq m_Z, \quad m_A + m_{H^\pm}, m_H + m_{H^\pm} \geq m_W. \tag{2.6}$$

We take into account following search results: direct bounds on the dark matter scattering from LUX experiment [34], LEP limit on the charged scalar mass of $m_{H^\pm} \geq 70$ GeV [35], exclusions from SUSY searches at LHC and LEP [17, 22] as well as the limit on the charged scalar width, $\Gamma_{tot} \geq 6.58 \times 10^{-18}$ GeV [14]. Finally, we require the agreement (at 2σ level) with electroweak precision observables [36–39] and with upper limit on relic density from Planck measurement, $\Omega_c h^2 \leq 0.1241$ [40].

¹See also [28, 29] for more detailed discussion

Benchmark Points

For our collider analysis we consider the set of benchmark points (BP) proposed in [14], which satisfy all the above mentioned constraints. These BP scenarios can be difficult for precise measurement at the LHC, due to small mass differences between new scalars, but should be clearly visible at the e^+e^- colliders. We consider

$$\text{BP 1: } m_H = 57.5 \text{ GeV}, \quad m_A = 113 \text{ GeV}, \quad m_{H^\pm} = 123 \text{ GeV},$$

$$\text{BP 2: } m_H = 85.5 \text{ GeV}, \quad m_A = 111 \text{ GeV}, \quad m_{H^\pm} = 140 \text{ GeV},$$

$$\text{BP 3: } m_H = 128 \text{ GeV}, \quad m_A = 134 \text{ GeV}, \quad m_{H^\pm} = 176 \text{ GeV}.$$

Our analysis is limited to the three low mass scenarios. The high mass scenarios are much more challenging as the production cross sections for signal events are very low and the observable decay products have low energies.

3 Software Setup

Signal events, i.e. pair produced charged and neutral scalars in e^+e^- collisions, are generated using CompHEP 4.5.2 [41, 42]. It uses IDM model files which are prepared using LanHEP 3.2 [43, 44]. The output of CompHEP in LHEF (Les Houches Event File) format is passed to PYTHIA 8.1.53 [45] for final state showering and multi-particle interactions. Background events are all generated by PYTHIA.

When generating the signal and background samples we include effects of the initial state radiation (ISR) but assume that accelerator beams are mono-energetic. We neglect beamstrahlung due to beam-beam interactions, which result in the additional energy smearing and increase the fraction of e^+e^- pairs colliding with lower energies, as it depends strongly on the accelerator design and assumed beam parameters. Using ILC beam spectra modeled with CIRCE1 [46] we estimated that the influence of beamstrahlung on the number of expected signal events was of the order of 1–3%. For the background processes increase of up to 10% in the event rate was observed.

Both signal and background event rates depend also on the expected polarization of the electron and positron beams. By a proper choice of the beam polarization one can significantly improve the signal to background ratio. However, possible degree of the beam polarization is determined by the accelerator design. Therefore, for the sake of generality, we consider unpolarized e^+e^- beams.

The jet reconstruction is performed by FASTJET 2.4.1 [47, 48] using anti-kt algorithm with a cone size of 0.4. To take into account the detector effects, we include acceptance cuts and simple modeling of the jet energy resolution [49]:

$$\frac{\sigma_E}{E} = \begin{cases} \frac{S}{\sqrt{E_j[\text{GeV}]}} & \text{for } E_j < 100 \text{ GeV}, \\ \frac{S}{\sqrt{100}} & \text{for } E_j \geq 100 \text{ GeV}, \end{cases} \quad (3.1)$$

where $\frac{\sigma_E}{E}$ is the relative jet energy uncertainty which is used to smear the measured jet energy and \mathcal{S} is the resolution parameter. The formula (3.1) describes well the energy resolution expected for single high energy jets when using algorithms based on so called particle flow [50]. Test data analysis and results of the detailed detector simulations based on GEANT4 indicate that the relative energy resolution of 3–4% should be feasible for highest jet energies both at ILC and CLIC, corresponding to parameter $\mathcal{S}=30\text{--}40\%$. However, the measurement precision is expected to deteriorate when we take into account the influence of beam related backgrounds and effects related to detector acceptance or event reconstruction. Therefore, we take a conservative value of $\mathcal{S}=50\%$ for our study. Final state leptons (electrons and muons) are assumed to be reconstructed without any sizable uncertainty, as determination of their momentum will be based on the track measurement. After signal and background events are generated and reconstructed, the analysis is carried out using ROOT 5.34 [51].

4 $e^+e^- \rightarrow H^+H^-$

In this section, the analysis of the charged scalar pair production process is considered for different benchmark scenarios and different final states. Two final states are considered for signal events ($\ell\nu jjHH$ and $jjjjHH$) and for each final state an independent analysis based on kinematic selection cuts is performed. The third final state, $\ell\nu\ell\nu HH$, is much more difficult as the two leptons come from different W^\pm and it is not possible to make use of kinematic constraints for efficient background suppression. Still, if the signal is observed in other channels, a dedicated analysis could be performed, based on single lepton energy spectra. In fig. 1, diagrams for charged scalar pair production with different decay channels are shown. In what follows, cross sections of signal and background processes are presented for two selected decay channels. Then, event generation and analysis are described in detail including selection cuts and their efficiencies.

4.1 Signal and Background Cross Sections

Cross sections of signal event production are calculated at leading order (LO) using a Monte Carlo simulation performed by CompHEP. For decay branching ratios of Standard Model particles like W and Z bosons, standard PDG values [52] are used. The charged scalar branching ratios are taken from 2HDMC 1.6.3 [53, 54]. Cross sections of background processes are calculated with PYTHIA. We consider the following background processes: W^+W^- pair production (WW), ZZ pair production (ZZ), fermion pair production from e^+e^- annihilation into single Z^*/γ^* (Z) and the top pair production (TT). Tables 1 and 2 show the LO signal and background cross sections at center of mass energies of 0.5 and 1 TeV, respectively.

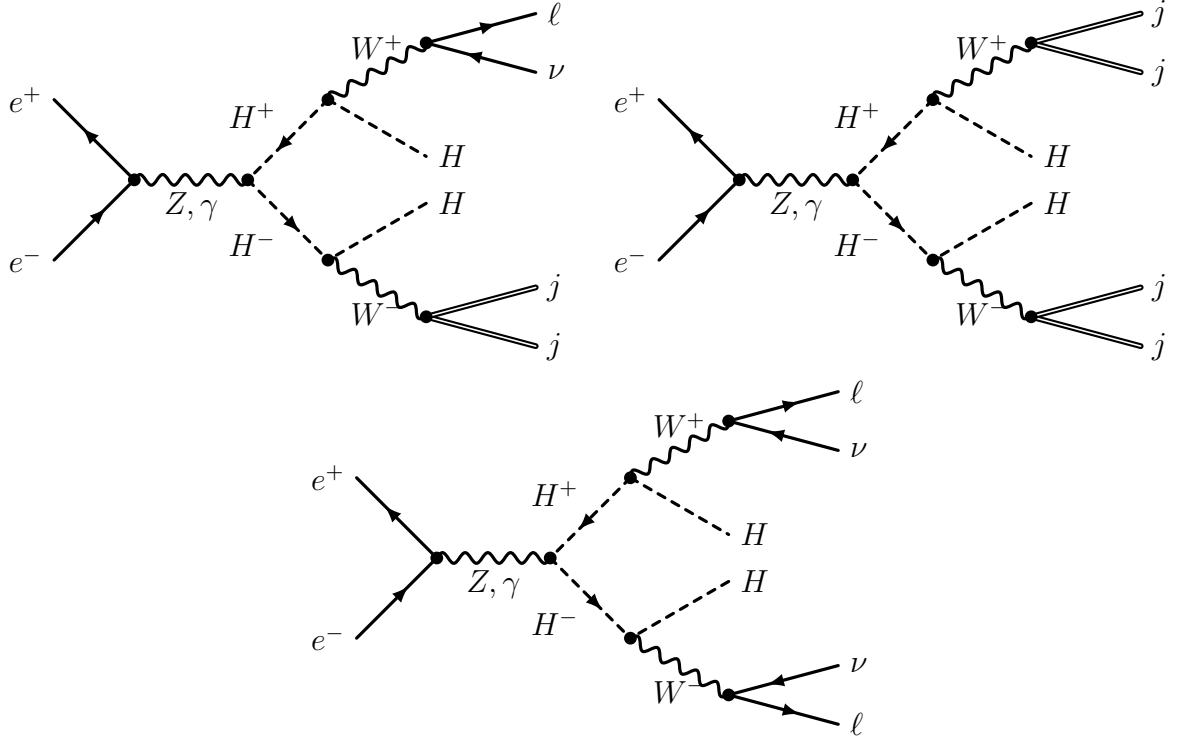


Figure 1: The Feynman diagrams for charged scalar pair production and decay processes, $e^+e^- \rightarrow (H^+H^- \rightarrow W^+W^-HH \rightarrow)\ell\nu jj HH$, $e^+e^- \rightarrow jjjj HH$ and $e^+e^- \rightarrow \ell\nu\ell\nu HH$.

4.2 Event Generation and Analysis

The charged scalar pair production, with subsequent decay $H^\pm \rightarrow W^\pm H$, where W boson decays either to a muon-neutrino or two light jet pairs, is generated using CompHep. Depending on the W boson decay channel, three final states are produced, i.e., $\ell\nu\ell\nu HH$, $\ell\nu jj HH$ and $jjjj HH$. These final states are labeled fully leptonic, semi-leptonic and fully hadronic, respectively. As mentioned above, we consider semi-leptonic and fully hadronic channels only, and an independent analysis based on kinematic selection cuts is performed for each final state. In what follows, the analysis and selection cuts of different final states are described in detail.

Process	H^+H^-			Background processes			
	BP1	BP2	BP3	WW	ZZ	Z	TT
Cross section [fb]	82.2	70.9	44.6	7807	583	16790	595

Table 1: Signal and background cross sections at $\sqrt{s} = 0.5$ TeV.

Process	H^+H^-			Background processes			
	BP1	BP2	BP3	WW	ZZ	Z	TT
Cross section [fb]	28.1	27.3	25.3	3180	233	4304	212

Table 2: Signal and background cross sections at $\sqrt{s} = 1$ TeV.

4.2.1 Semi-leptonic Final State

Signal events are characterized by a single lepton and two light jets from W boson decays, and missing transverse momentum. Therefore, we require to have one lepton and two jets passing a 10 GeV transverse energy threshold reconstructed in the event. The threshold cut is applied to reject events with soft leptons or jets in their final state and the same cut is applied at both center of mass energies, $\sqrt{s} = 0.5$ and 1 TeV. Although a harder cut could be adopted at 1 TeV collisions, the current set of selection cuts gives a reasonable background suppression while limiting the loss of statistics in signal selection. The jet energy threshold is set to avoid uncertainties in soft jet energy measurement due to the jet reconstruction algorithm and detector effects. The threshold of missing transverse momentum is taken to be 20 GeV for the two center of mass energies. This cut is most useful for suppression of single or pair production of Z bosons.

For all benchmark scenarios considered in our analysis the scalar mass difference $m_{H^\pm} - m_H$ is significantly smaller than the nominal W^\pm boson mass. For signal events, two jets observed in semi-leptonic channel come from the decay of the off-shell W^\pm boson (W^*), with two jet invariant mass corresponding to the W^* virtuality. On the other hand, the sum of jet energies measured in the laboratory frame is given by a product of the W^* virtuality (i.e. the energy in the W^* rest frame) and the Lorentz boost factor γ corresponding to the W^* velocity in the laboratory frame. The Lorentz boost of W^* is unknown, but we expect that W^* production with the highest possible virtuality is most likely. In such a case, W^* is almost at rest in the reference frame of decaying H^\pm , and we can use the Lorentz boost factor of charged scalar for transformation of jet energies. As the energies of the charged scalars are given by the beam energy, their Lorentz boost factor is uniquely defined by their mass: $\gamma = E_{beam}/M_{H^\pm}$. Therefore we expect to observe a narrow peak not only for the two jet invariant mass but also in the sum of two jet energies distribution. This is clearly seen in figs. 2a and 2b, where the sum of two jet energies is plotted versus their invariant mass, for benchmark scenario BP1 (red dots). For comparison, semi-leptonic background events $e^+e^- \rightarrow W^+W^-$, dominated by on-shell W^\pm boson decays, are also shown. The peak observed for signal events is clearly shifted with respect to the background event distribution, both in the energy and in the invariant mass, and this observation can be used for efficient suppression of background events.

It should be mentioned that background events in the semi-leptonic channel can

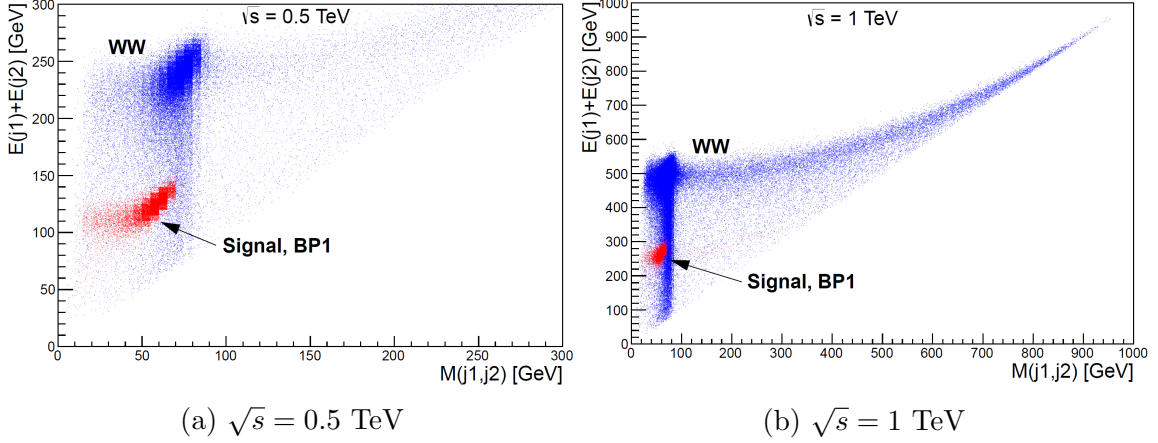


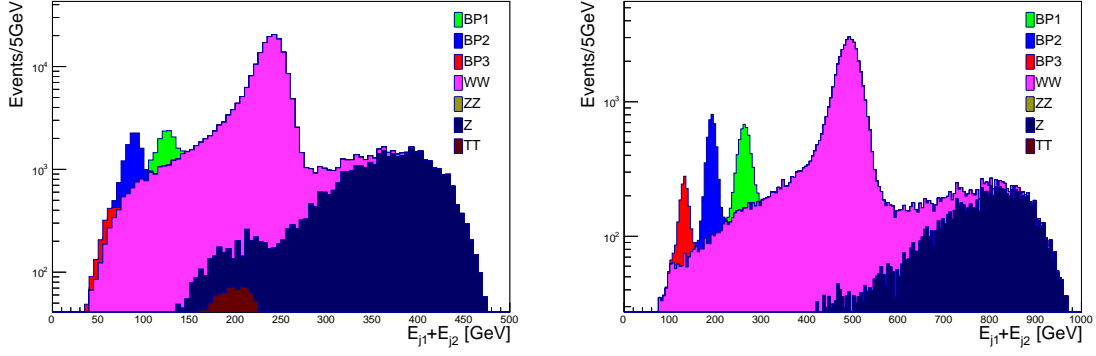
Figure 2: Correlation for $e^+e^- \rightarrow H^+H^-$ between the sum of energies of two jets and their invariant mass at $\sqrt{s} = 0.5$ TeV (left) and 1 TeV (right). The comparison is only between the semi-leptonic signal (BP1) and WW background.

also be suppressed by a cut on the missing mass, i.e. on invariant mass of the final state particles escaping detection, reconstructed from the energy-momentum conservation [24]. For signal events the missing mass is at least twice the H boson mass, whereas for $e^+e^- \rightarrow W^+W^-$ events (in semi-leptonic decay channel) its distribution should be peaked at small masses, corresponding to a single escaping neutrino. However, the cut on the missing mass is strongly correlated with the jet energy and invariant mass cuts and therefore the resulting improvement in the event selection is marginal. We do not use this cut for the presented results.

We found that the jet energy sum distribution itself, as shown in figs. 3a and 3b gives good signal and background separation. As described above, the distribution is softer for signal events due to the smaller W^\pm boson virtuality and smaller Lorentz boost factor. For background events, like WW and ZZ pair production, the two-jet energy is the energy of the parent boson, which is half of the collision energy.

Based on figs. 2a and 2b, a cut on the sum of jet energies is applied for semi-leptonic events, of 150(350) GeV for $\sqrt{s} = 0.5(1)$ TeV center of mass energy. Table 3 gives a summary of selection cuts for this final state while tables 4 and 5 present selection efficiencies for signal and background processes at $\sqrt{s} = 0.5$ and 1 TeV, respectively.

Invariant mass distribution of the two jets, obtained after applying the cut on the sum of the two jet energies, is plotted in fig. 4a (4b) for signal and background events at $\sqrt{s} = 0.5$ TeV (1 TeV). These plots are used to obtain information about the mass difference $m_{H^\pm} - m_H$ with statistical uncertainty below 100 MeV (see discussion in section 6). Using a mass window cut the final numbers of signal (S) and background (B) events can be extracted, as well as the signal significance $s = S/\sqrt{S+B}$, as shown in table 6. Significance of the signal observation is very high even for the least



(a) $e^+e^- \rightarrow \ell\nu jj HH$ at $\sqrt{s} = 0.5$ TeV

(b) $e^+e^- \rightarrow \ell\nu jj HH$ at $\sqrt{s} = 1$ TeV

Figure 3: Sum of two jets energies in semileptonic final state at $\sqrt{s} = 0.5$ TeV (left) and 1 TeV (right), for $e^+e^- \rightarrow H^+H^-$.

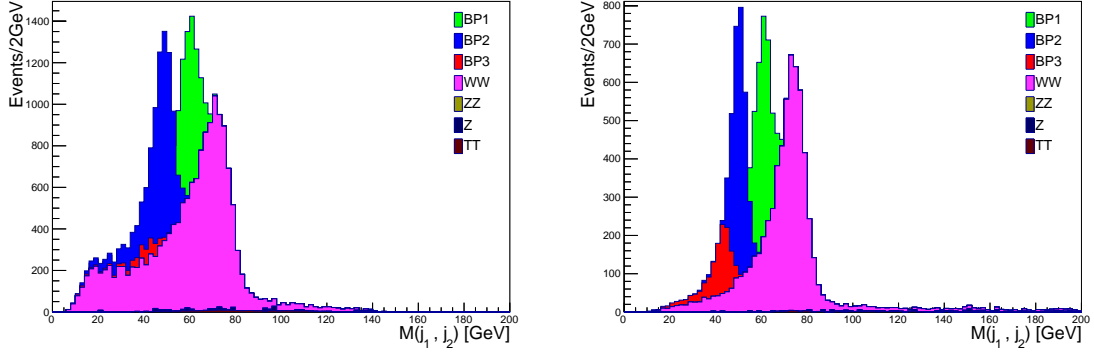
favoured benchmark point, BP3. The corresponding precision of the signal cross section determination is 2–12% for $\sqrt{s} = 0.5$ TeV and 2–4% for $\sqrt{s} = 1$ TeV.

H^+H^- analysis, semi-leptonic final state selection		
Selection cut	$\sqrt{s} = 0.5$ TeV	$\sqrt{s} = 1$ TeV
One lepton	$E_T > 10$ GeV	$E_T > 10$ GeV
Two jets	$E_T > 10$ GeV	$E_T > 10$ GeV
p_T^{miss}	$p_T^{\text{miss}} > 20$ GeV	$p_T^{\text{miss}} > 20$ GeV
$E(j_1) + E(j_2)$	$E(j_1) + E(j_2) < 150$ GeV	$E(j_1) + E(j_2) < 350$ GeV

Table 3: Selection cuts for semi-leptonic final state analysis at two center of mass energies of 0.5 and 1 TeV.

H^+H^- analysis, semi-leptonic final state selection							
Cut eff.	BP1	BP2	BP3	WW	ZZ	Z	TT
One Lepton	0.89	0.93	0.77	0.45	0.13	0.069	0.67
Two Jets	0.67	0.78	0.53	0.49	0.23	0.25	0.027
p_T^{miss}	0.83	0.88	0.49	0.78	0.061	0.35	0.92
$E(j_1) + E(j_2)$	1	1	1	0.08	0.12	0.0065	0.18
Total eff.	0.5	0.64	0.2	0.014	0.00021	3.9e-05	0.0029

Table 4: Cut efficiencies for semi-leptonic final state analysis at center of mass energy of 0.5 TeV.



(a) $e^+e^- \rightarrow \ell\nu jjHH$ at $\sqrt{s} = 0.5$ TeV

(b) $e^+e^- \rightarrow \ell\nu jjHH$ at $\sqrt{s} = 1$ TeV

Figure 4: Invariant mass of two jets in semileptonic final state at $\sqrt{s} = 0.5$ TeV (left) and 1 TeV (right), for $e^+e^- \rightarrow H^+H^-$.

H^+H^- analysis, semi-leptonic final state selection							
Cut eff.	BP1	BP2	BP3	WW	ZZ	Z	TT
One Lepton	0.95	0.97	0.95	0.28	0.11	0.063	0.57
Two Jets	0.87	0.91	0.68	0.47	0.21	0.23	0.024
p_T^{miss}	0.97	0.97	0.9	0.86	0.14	0.51	0.93
$E(j_1) + E(j_2)$	1	1	1	0.12	0.11	0.013	0.25
Total eff.	0.8	0.86	0.59	0.014	0.00035	9.6e-05	0.0032

Table 5: Cut efficiencies for semi-leptonic final state analysis at center of mass energy of 1 TeV.

H^+H^- , semi-leptonic final state at $\mathcal{L} = 500 \text{ fb}^{-1}$								
	$\sqrt{s} = 0.5 \text{ TeV}$				$\sqrt{s} = 1 \text{ TeV}$			
	S	B	S/B	$S/\sqrt{S+B}$	S	B	S/B	$S/\sqrt{S+B}$
BP 1	5101	6136	0.83	48	3055	1901	1.6	43
BP 2	4885	2285	2.1	58	2590	461	5.6	47
BP 3	474	2784	0.17	8.3	861	433	2.0	24

Table 6: Number of events in signal and background processes after all selection cuts at integrated luminosity of 500 fb^{-1} . S and B stand for the number of signal and background events.

4.2.2 Fully Hadronic Final State

Signal events are characterized by four light jets from off-shell W bosons decays and missing transverse momentum. An event is required to have four jets passing 10 GeV transverse energy threshold, both for $\sqrt{s} = 0.5$ and 1 TeV. Contrary to the case of

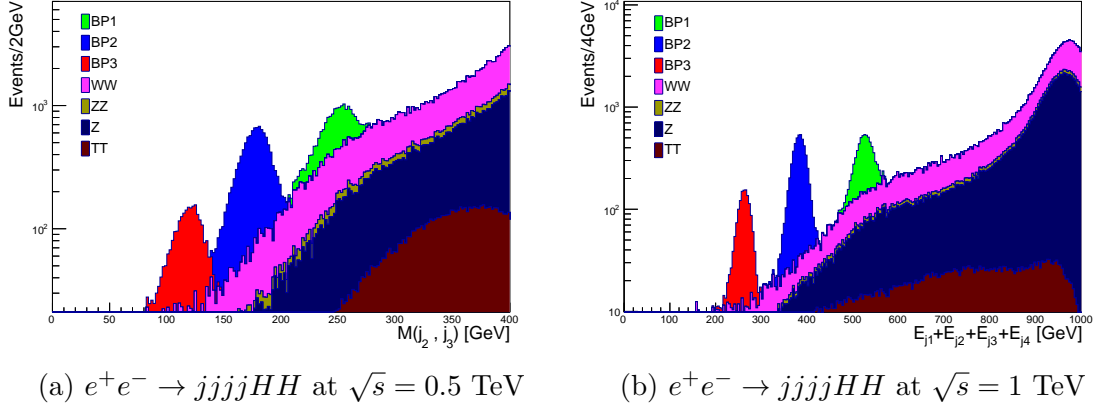


Figure 5: Sum of four jets energies in fully hadronic final state at $\sqrt{s} = 0.5$ TeV (left) and 1 TeV (right), for $e^+e^- \rightarrow H^+H^-$.

semi-leptonic final state, there is no p_T^{miss} within the detector resolution due to the back-to-back configuration of H bosons which results in cancellation of their effect in p_T^{miss} calculation. Therefore the missing transverse momentum is required to be less than 10 GeV. The sum of energies of the four jets in the event is required to be less than 300(600) GeV at $\sqrt{s} = 0.5(1)$ TeV respectively. This cut is applied following the same strategy as described in the semi-leptonic case using a two dimensional correlation plot. The distributions of the sum of energies of the four jets are shown in figs. 5a and 5b, where in case of background events like WW and ZZ , the four jet energy is consistent with the collision energy and is expected to dominate the region near 0.5 or 1 TeV, depending on center of mass energy. Table 7 summarizes selection cuts while tables 8 and 9 present selection efficiencies for signal and background processes at $\sqrt{s} = 0.5$ and 1 TeV, respectively.

H^+H^- analysis, fully hadronic final state selection		
Selection cut	$\sqrt{s} = 0.5$ TeV	$\sqrt{s} = 1$ TeV
4 jets	$E_T > 10$ GeV	$E_T > 10$ GeV
p_T^{miss}	$p_T^{\text{miss}} < 10$ GeV	$p_T^{\text{miss}} < 10$ GeV
$\sum_{i=1}^4 E(j_i)$	$\sum_{i=1}^4 E(j_i) < 300$ GeV	$\sum_{i=1}^4 E(j_i) < 600$ GeV

Table 7: Selection cuts for fully hadronic final state analysis at two center of mass energies of 0.5 and 1 TeV.

When the cut on the sum of four jets energies is applied, the invariant mass of pairs of jets can be investigated. As described in section 4.2.1, both W^* bosons are likely to be produced with the same virtuality and with the same Lorentz boost factor as for H^\pm . As the sum of energies for both jet pairs is expected to be the

H^+H^- analysis, fully hadronic final state selection							
Cut eff.	BP1	BP2	BP3	WW	ZZ	Z	TT
Four Jets	0.48	0.57	0.42	0.19	0.23	0.049	0.1
p_T^{miss}	1	1	1	0.94	0.83	0.88	0.69
$\sum_{i=1}^4 E(j_i)$	1	1	1	0.053	0.065	0.036	0.25
Total eff.	0.48	0.57	0.42	0.0095	0.012	0.0016	0.018

Table 8: Cut efficiencies for fully hadronic final state analysis at center of mass energy of 0.5 TeV.

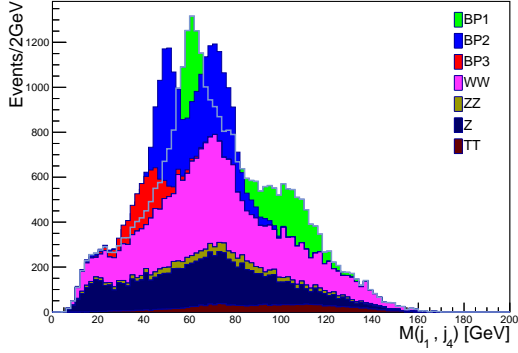
H^+H^- analysis, fully hadronic final state selection							
Cut eff.	BP1	BP2	BP3	WW	ZZ	Z	TT
Four Jets	0.77	0.81	0.54	0.11	0.15	0.055	0.11
p_T^{miss}	0.86	0.93	0.9	0.91	0.76	0.84	0.61
$\sum_{i=1}^4 E(j_i)$	1	1	1	0.045	0.051	0.037	0.25
Total eff.	0.66	0.75	0.48	0.0045	0.0058	0.0017	0.017

Table 9: Cut efficiencies for fully hadronic final state analysis at center of mass energy of 1 TeV.

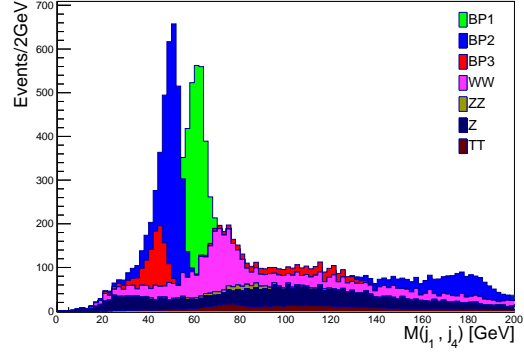
same, the jet with the highest energy in the laboratory reference frame should be matched to the jet with the lowest energy. Consequently, the second and third jet should be matched to reconstruct the other W boson in the event. The described matching is not fully efficient as detector effects can disturb the jet energy ordering. More detailed analysis, based on the so called kinematic fit² approach, would allow to select the correct (most probable) jet matching with higher efficiency. This is beyond the scope of present analysis.

Figures 6a and 6b show the invariant mass of the first and fourth jet pairs (j_1j_4) at $\sqrt{s} = 0.5$ TeV and 1 TeV, respectively. The corresponding distributions for second and third jet pairs (j_2j_3) are shown in figs. 7a and 7b, respectively. As seen in figs. 6a and 7a there is a low value peak which should be related to the right combinations of jets and a second bump related to wrong matching. In case of 1 TeV collisions the second bump is much smaller. These plots are used for signal extraction using a mass window cut. Tables 10 and 11 show number of signal and background

²In the kinematic fit procedure all possible jet combinations are considered. Each hypothesis is compared with the expected event topology and kinematic constraints, taking into account the detector resolution, acceptance and reconstruction efficiency, based on the detailed simulation of detector effect. The likelihood value is calculated for each combination and the hypothesis with the highest likelihood is selected for the analysis as the proper one.

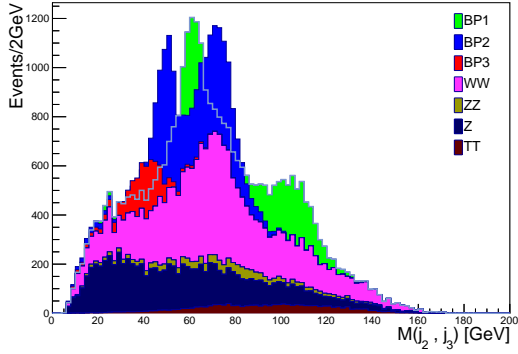


(a) $e^+e^- \rightarrow jjjjHH$ at $\sqrt{s} = 0.5$ TeV

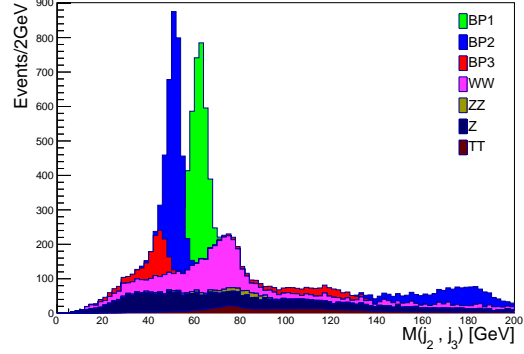


(b) $e^+e^- \rightarrow jjjjHH$ at $\sqrt{s} = 1$ TeV

Figure 6: Invariant mass of the first and fourth jet in fully hadronic final state at $\sqrt{s} = 0.5$ TeV (left) and 1 TeV (right), for $e^+e^- \rightarrow H^+H^-$.



(a) $e^+e^- \rightarrow jjjjHH$ at $\sqrt{s} = 0.5$ TeV



(b) $e^+e^- \rightarrow jjjjHH$ at $\sqrt{s} = 1$ TeV

Figure 7: Invariant mass of the second and third jet in fully hadronic final state at $\sqrt{s} = 0.5$ TeV (left) and 1 TeV (right), for $e^+e^- \rightarrow H^+H^-$.

events, signal to background ratio and the signal significance expected for integrated luminosity of 500 fb^{-1} , based on a mass window cut on invariant mass of jet pairs, i.e., $m(j_1j_4)$ and $m(j_2j_3)$ respectively. If the kinematic fit method was used for selecting proper jet matching, both invariant mass distributions could be used to get even better signal to background separation. However, we have found, that already with the single invariant mass distribution, very high signal selection significance can be obtained. The corresponding precision of the signal cross section determination is of the order of 2–6%. Furthermore the position of the peak observed in the invariant mass distribution can be used to constrain the mass difference $m_{H^\pm} - m_H$. Similar to the semi-leptonic channel, very high statistical precision of the order of 100 MeV is expected (see discussion in section 6).

H^+H^- , fully hadronic final state at $\mathcal{L} = 500 \text{ fb}^{-1}$, cut on $m(j_1j_4)$								
	$\sqrt{s} = 0.5 \text{ TeV}$				$\sqrt{s} = 1 \text{ TeV}$			
	S	B	S/B	$S/\sqrt{S+B}$	S	B	S/B	$S/\sqrt{S+B}$
BP 1	4160	6742	0.61	40	2967	1040	2.8	47
BP 2	3751	3771	0.99	43	2450	473	5.2	45
BP 3	1543	4040	0.38	21	625	668	0.9	17

Table 10: Number of events in signal and background processes after all selection cuts as in tables 8 and 9 plus a mass window cut on $m(j_1j_4)$ at integrated luminosity of 500 fb^{-1} . S and B stand for the number of signal and background events.

H^+H^- , fully hadronic final state at $\mathcal{L} = 500 \text{ fb}^{-1}$, cut on $m(j_2j_3)$								
	$\sqrt{s} = 0.5 \text{ TeV}$				$\sqrt{s} = 1 \text{ TeV}$			
	S	B	S/B	$S/\sqrt{S+B}$	S	B	S/B	$S/\sqrt{S+B}$
BP 1	3764	6210	0.6	38	3137	1598	2.0	45
BP 2	3445	3645	0.9	41	2176	855	2.5	39
BP 3	1473	4374	0.3	19	627	1109	0.6	15

Table 11: Number of events in signal and background processes after all selection cuts as in tables 8 and 9 plus a mass window cut on $m(j_2j_3)$ at integrated luminosity of 500 fb^{-1} . S and B stand for the number of signal and background events.

5 $e^+e^- \rightarrow AH$

The production of pairs of neutral scalars, presented in this section, is analysed with the same computational setup as discussed in the previous section. In all three benchmark points, the branching ratio of A to ZH , $BR(A \rightarrow ZH)$, is close to 100%. Therefore the considered signal events are $e^+e^- \rightarrow AH \rightarrow ZHH$. For the Z boson decay channel, two different final states are taken into account, i.e. the leptonic final state, where Z decays to a pair of electrons or muons, and hadronic final state where Z decays to two jets. Therefore two final states, leptonic and hadronic, are considered in each mass scenario for center of mass energies of 0.5 and 1 TeV. Figure 8 shows the signal production process. We will first present the cross section calculation for these processes, followed by the detailed description of event selection and analysis.

5.1 Signal and Background Cross Sections

Signal cross section for different scenarios is calculated with CompHep using Monte Carlo approach. Table 12 shows cross sections at center of mass energies of 0.5 and 1 TeV. The same set of background events is used in the analysis for both final states. However, events are selected with the final states compatible with the considered

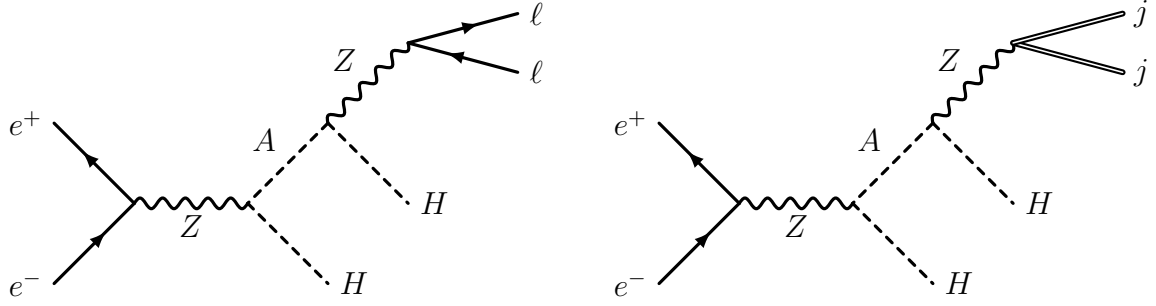


Figure 8: The Feynman diagrams for our production and decay processes, $e^+e^- \rightarrow HA \rightarrow HHZ \rightarrow \ell\ell HH$ and $e^+e^- \rightarrow HA \rightarrow HHZ \rightarrow jj HH$.

Process	$e^+e^- \rightarrow AH$					
	$\sqrt{s} = 0.5 \text{ TeV}$			$\sqrt{s} = 1 \text{ TeV}$		
Benchmark point	BP1	BP2	BP3	BP1	BP2	BP3
Cross section [fb]	45	42.9	34.2	12.5	12.4	11.8

Table 12: Signal and background cross sections at $\sqrt{s} = 0.5 \text{ TeV}$.

signal process: for leptonic(hadronic) final state analysis, the W and Z boson from the background sample are also assumed to decays to leptons (jets).

5.1.1 Leptonic Final State

In the leptonic final state analysis signal events contain two leptons, which are taken to be electrons or muons, and missing transverse momentum (due to escaping HH pair). The WW background has to involve $W \rightarrow \ell\nu$ decay for both W bosons in order to produce two (same flavour) leptons. In such case, the sum of energies of those leptons is usually higher than that in the signal events because these leptons stem from high energy W bosons, while for signal events they come from a single off-shell Z boson, with much lower Lorentz boost. For signal events, we also expect to observe the peak in the invariant mass distribution of the lepton pair, which corresponds to the $m_A - m_H$ mass difference.

The ZZ background can have one of or both Z bosons decaying to lepton pairs, i.e., $ZZ \rightarrow \ell\ell jj$ or $ZZ \rightarrow \ell\ell\ell\ell$. The first type of events can be easily suppressed by a jet veto cut, while, the second type is reduced by the cut on the number of leptons. The ZZ background with one of the bosons decaying to neutrinos $ZZ \rightarrow \ell\ell\nu\nu$ and the Drell-Yan (single Z^*/γ^*) background can be suppressed by rejecting events with the invariant mass of the lepton pair is consistent with Z mass.

Summarized in table 13 are the cuts used for selection of signal events in the leptonic channel. An event is required to have two leptons with transverse energies above 1(5) GeV at $\sqrt{s} = 0.5(1) \text{ TeV}$. The missing transverse momentum is required to be in the range $10 < p_T^{\text{miss}} < 120(250) \text{ GeV}$ at $\sqrt{s} = 0.5(1) \text{ TeV}$. The lower

limit is applied to reject the Drell-Yan background, while, the upper limit is for suppression of WW and ZZ events. Finally, the invariant mass of the lepton pair is required to be outside the mass window of $m_Z \pm 20$ GeV where $m_Z=90$ GeV. In case of signal events, the invariant mass of the lepton pair is expected to be peaked at $m_A - m_H$, which is much below m_Z . Tables 14 and 15 show selection efficiencies for leptonic channel at $\sqrt{s} = 0.5$ and 1 TeV, respectively.

<i>HA</i> analysis, leptonic final state selection		
Selection cut	$\sqrt{s} = 0.5$ TeV	$\sqrt{s} = 1$ TeV
2 leptons	$E_T > 1$ GeV	$E_T > 5$ GeV
p_T^{miss}	$10 < p_T^{\text{miss}} < 120$ GeV	$10 < p_T^{\text{miss}} < 250$ GeV
m_{ℓ_1, ℓ_2}	$ m_{\ell_1, \ell_2} - m_Z > 20$ GeV	$ m_{\ell_1, \ell_2} - m_Z > 20$ GeV

Table 13: Selection cuts for leptonic final state analysis at two center of mass energies of 0.5 and 1 TeV.

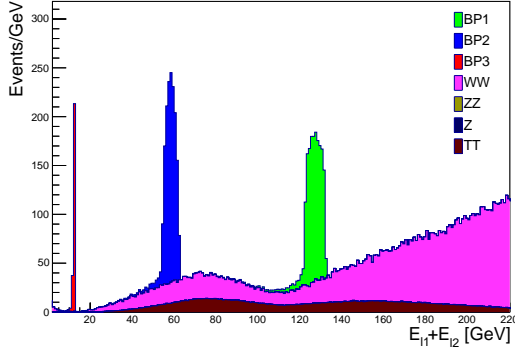
<i>HA</i> analysis, leptonic final state selection							
Cut eff.	BP1	BP2	BP3	WW	ZZ	Z	TT
Two Leptons	0.99	1	0.92	0.76	0.083	0.8	0.4
p_T^{miss}	1	1	0.24	0.91	0	3.9e-05	0.89
Z suppression	1	1	1	0.97	-	0.48	0.73
Total eff.	0.99	1	0.22	0.67	0	1.5e-05	0.26

Table 14: Cut efficiencies for leptonic final state analysis at the center of mass energy of 0.5 TeV.

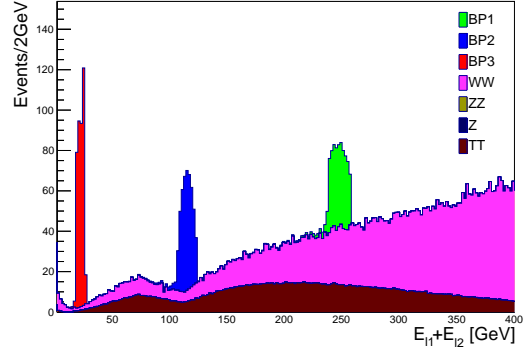
<i>HA</i> analysis, leptonic final state selection							
Cut eff.	BP1	BP2	BP3	WW	ZZ	Z	TT
Two Leptons	0.98	0.98	0.65	0.5	0.19	0.66	0.52
p_T^{miss}	1	1	1	0.92	2.1e-05	0.0001	0.96
Z suppression	1	1	1	0.98	0.5	0.63	0.86
Total eff.	0.98	0.98	0.65	0.45	2e-06	4.2e-05	0.42

Table 15: Cut efficiencies for leptonic final state analysis at the center of mass energy of 1 TeV.

The final signal event selection may be based on the sum of energies of the lepton pair (figs. 9a and 9b) or on the invariant mass distribution (figs. 10a and 10b), since both show clear separation between signal and background processes. As leptons

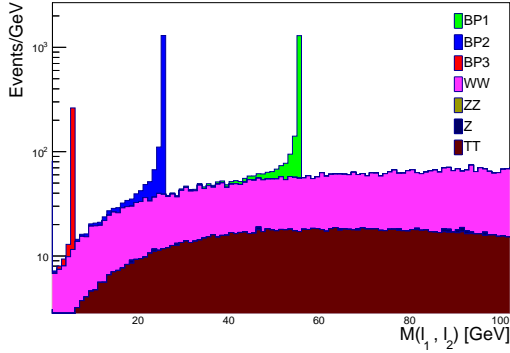


(a) $e^+e^- \rightarrow \ell\ell HH$ at $\sqrt{s} = 0.5$ TeV

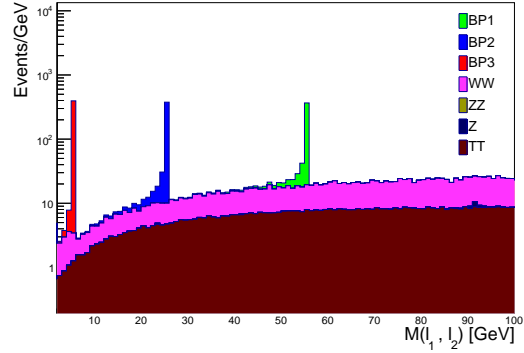


(b) $e^+e^- \rightarrow \ell\ell HH$ at $\sqrt{s} = 1$ TeV

Figure 9: Sum of energies of two leptons in leptonic final state at $\sqrt{s} = 0.5$ TeV (left) and 1 TeV (right), for $e^+e^- \rightarrow HA$.



(a) $e^+e^- \rightarrow \ell\ell HH$ at $\sqrt{s} = 0.5$ TeV



(b) $e^+e^- \rightarrow \ell\ell HH$ at $\sqrt{s} = 1$ TeV

Figure 10: Invariant mass of the lepton pair in leptonic final state at $\sqrt{s} = 0.5$ TeV (left) and 1 TeV (right), for $e^+e^- \rightarrow HA$.

are reconstructed with a high efficiency and very good momentum resolution, a very sharp edge should be observed in the invariant mass distributions, which can be used to reconstruct the value of $m_A - m_H$ with negligible statistical uncertainty (see discussion in section 6). Applying a mass window cut on invariant mass distributions of figs. 10a and 10b, the numbers of signal and background events are counted to estimate the signal significance as shown in table 16. The corresponding precision of the signal cross section determination is 3–7%.

5.1.2 Hadronic Final State

In the hadronic final state, signal events contain two jets from the off-shell Z decay and missing transverse momentum from the escaping HH pair. The analysis follows the same strategy, as described above for the leptonic final state.

HA , leptonic final state at $\mathcal{L} = 500 \text{ fb}^{-1}$								
	$\sqrt{s} = 0.5 \text{ TeV}$				$\sqrt{s} = 1 \text{ TeV}$			
	S	B	S/B	$S/\sqrt{S+B}$	S	B	S/B	$S/\sqrt{S+B}$
BP 1	1382	279	4.9	34	386	55	7	18
BP 2	1378	186	7.4	35	397	30	13	19
BP 3	256	81	3.1	14	257	51	5	15

Table 16: Number of events in signal and background processes after all selection cuts at integrated luminosity of 500 fb^{-1} .

An event is required to have two jets reconstructed with transverse energies above 5 GeV. The missing transverse momentum is required to be in the range $10 < p_T^{\text{miss}} < 120(250) \text{ GeV}$, for $\sqrt{s} = 0.5(1) \text{ TeV}$, following the same reasoning as described above for the leptonic final state. However, the precision of the invariant mass reconstruction is much poorer for two jets than it is for two leptons. Therefore, instead of a cut on the invariant mass of the jet pair, we require that the sum of jet energies is less than 150(300) GeV at $\sqrt{s} = 0.5(1) \text{ TeV}$. This constrain replaces the cut on the invariant mass of the jet pair and real Z boson suppression cut. Table 17 lists a summary of selection cuts for the hadronic final state while tables 18 and 19 show selection efficiencies at $\sqrt{s} = 0.5$ and 1 TeV, respectively. High signal selection efficiency is obtained, except for the BP3 scenario which can hardly be observed in the hadronic channel at $\sqrt{s} = 0.5 \text{ TeV}$.

Figures 11a and 11b show the distributions of the sum of jet energies in signal and background events. These plots justify the cut on the energy sum described above. The invariant mass distributions of the jet pairs are shown in figs. 12a and 12b. These distributions are used for the final event selection with a mass window cut. Table 20 summarizes the results obtained by counting the number of signal and background events after final selection and mass window cuts.

HA analysis, hadronic final state selection		
Selection cut	$\sqrt{s} = 0.5 \text{ TeV}$	$\sqrt{s} = 1 \text{ TeV}$
2 jets	$E_T > 5 \text{ GeV}$	$E_T > 5 \text{ GeV}$
p_T^{miss}	$10 < p_T^{\text{miss}} < 120 \text{ GeV}$	$10 < p_T^{\text{miss}} < 250 \text{ GeV}$
$E(j_1) + E(j_2)$	$E(j_1) + E(j_2) < 150 \text{ GeV}$	$E(j_1) + E(j_2) < 300 \text{ GeV}$

Table 17: Selection cuts for hadronic final state analysis at two center of mass energies of 0.5 and 1 TeV.

<i>HA</i> analysis, hadronic final state selection							
Cut eff.	BP1	BP2	BP3	WW	ZZ	Z	TT
Two Jets	0.67	0.78	0.0027	0.033	0.036	0.36	2e-06
p_T^{miss}	1	1	0.91	0.018	0.066	0.061	0
$E(j_1) + E(j_2)$	1	1	1	0.16	0.19	0.19	0
Total eff.	0.67	0.78	0.0025	9.5e-05	0.00045	0.0041	0

Table 18: Cut efficiencies for hadronic final state analysis at center of mass energy of 0.5 TeV.

<i>HA</i> analysis, hadronic final state selection							
Cut eff.	BP1	BP2	BP3	WW	ZZ	Z	TT
Two Jets	0.87	0.76	0.14	0.22	0.14	0.24	2.5e-05
p_T^{miss}	1	1	1	0.028	0.089	0.073	0.2
$E(j_1) + E(j_2)$	1	1	1	0.078	0.14	0.17	0
Total eff.	0.87	0.76	0.14	0.00049	0.0018	0.003	0

Table 19: Cut efficiencies for hadronic final state analysis at center of mass energy of 1 TeV.

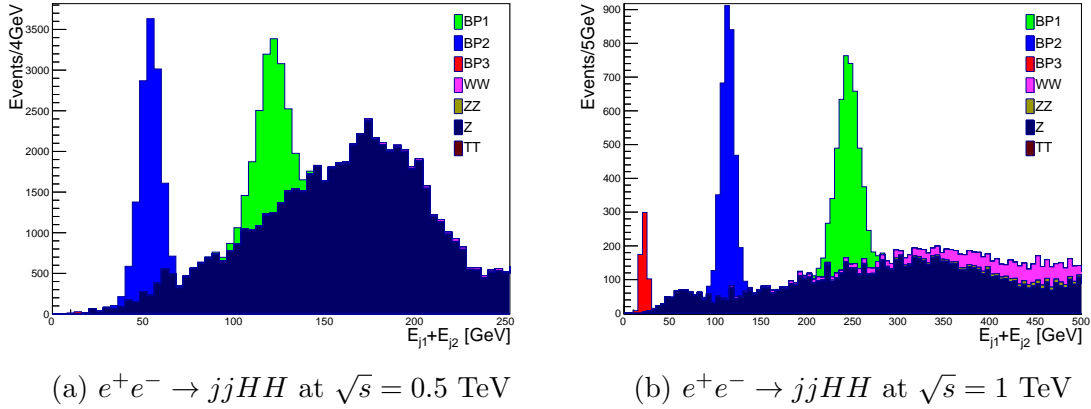


Figure 11: Sum of two jets energies in hadronic final state at $\sqrt{s} = 0.5$ TeV (left) and 1 TeV (right), for $e^+e^- \rightarrow HA$.

6 Dark Matter Mass Measurement

As shown above, the energy and invariant mass distributions for signal events show clear peaks, which result from the kinematic constraints of the considered scenario and can be related to the scalar masses. In this section, we propose a procedure for determination of charged and neutral scalar masses and estimate the statistical precision, which can be reached at e^+e^- collider with 500 fb^{-1} . Feasibility of mass and

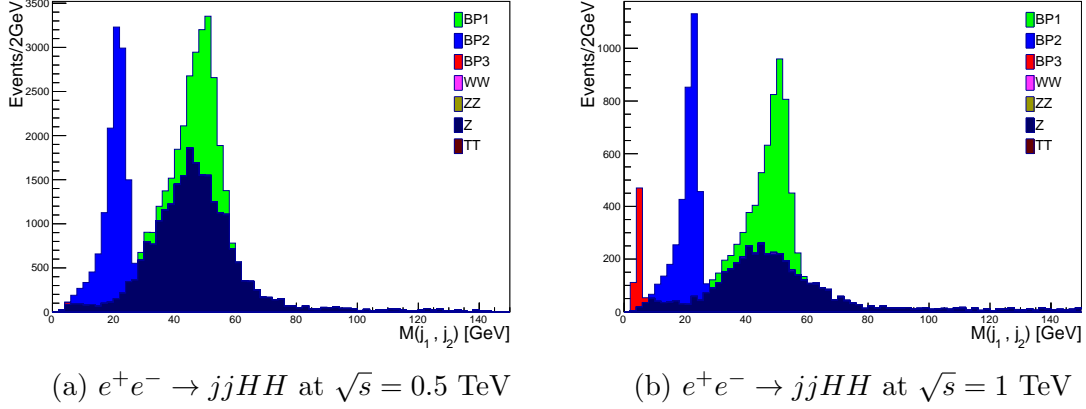


Figure 12: Invariant mass of the two jets in hadronic final state at $\sqrt{s} = 0.5$ TeV (left) and 1 TeV (right), for $e^+e^- \rightarrow HA$.

HA , hadronic final state at $\mathcal{L} = 500 \text{ fb}^{-1}$								
	$\sqrt{s} = 0.5 \text{ TeV}$				$\sqrt{s} = 1 \text{ TeV}$			
	S	B	S/B	$S/\sqrt{S+B}$	S	B	S/B	$S/\sqrt{S+B}$
BP 1	3972	3926	1.0	45	2693	1074	2.5	44
BP 2	7011	709	9.9	80	2880	199	14	52
BP 3	30	195	0.15	2	399	8	49	20

Table 20: Number of events in signal and background processes after all selection cuts at integrated luminosity of 500 fb^{-1} . S and B stand for the number of signal and background events.

spin measurement of IDM scalars, in particular of the DM candidate, were already studied for the e^+e^- collider, see e.g. [24]. However, the approach presented in [24] focuses on the single particle distributions,

which we consider challenging from the experimental point of view. In particular, lepton energy distributions have to be measured down to very low energies, of the order of few GeV. It requires efficient identification of low energy leptons and very good background understanding.

We propose an approach, which makes use of the reconstructed peaks in the energy and invariant mass distributions. The approach is based on the observation that the off-shell W^* and Z^* bosons are most likely produced with their virtualities close to the maximum allowed values given by the mass differences $m_{H^\pm} - m_H$ and $m_A - m_H$, respectively.

First, we consider the distribution of the sum of energies of the two jets, in the semi-leptonic final state of charged scalar production, $\sum_{i=1}^2 E(j_i)$. In the W^* boson rest frame, the sum of jet energies is equal to the W^* boson mass and its

most probable value is given by $m_{H^\pm} - m_H$. When produced with close to maximal virtuality, the W^* boson is almost at rest in the reference frame of decaying H^\pm . Therefore the Lorentz boost applied to jet energies can be approximated by the H^\pm boost. It can be shown that in this approximation

$$\sum_{i=1}^2 E(j_i) = E_{beam} \left(1 - \frac{m_H}{m_{H^\pm}} \right) . \quad (6.1)$$

Defining $R = \frac{m_H}{m_{H^\pm}}$, one can solve eq. (6.1) to obtain

$$R = 1 - \frac{\sum_{i=1}^2 E(j_i)}{E_{beam}} . \quad (6.2)$$

To reconstruct the most probable value of the jet energy sum, which should be use in eq. (6.2), the distribution was fitted with a Gaussian function assuming the background probability density function (p.d.f) is well known from simulation. Equation (6.2) can be then used to calculate the values of m_H/m_{H^\pm} for each channel. In case of the four jet final state (fully hadronic final state for charged scalar pair production), the four jet energy sum can be divided by two to get the proper estimate of the jet pair energy. An average value of R can be then calculated, based on all considered channels.

In the next step, we consider the invariant mass distributions for the two jets of the semi-leptonic final state in charged scalar production, $m(j_1, j_2)$. As already mentioned above, this distribution is expected to peak at the most probable W^* boson virtuality, which is

$$m(j_1, j_2) = m_{H^\pm} - m_H . \quad (6.3)$$

As before, we apply a Gaussian fit on signal plus background distributions to obtain the signal peak position. This procedure can be also used for two jet or two lepton invariant mass distribution for the neutral scalar pair production events, providing the value of $m_A - m_H$. Using the average value of m_H/m_{H^\pm} (denoted as R) obtained from the first step and $m_{H^\pm} - m_H$ average value from the second step (based on charged scalar production analysis results), we can extract H and H^\pm masses for each considered scenario.

Finally, we consider the invariant mass distributions for the two leptons of the leptonic final state and for the two jets of the hadronic final state, in neutral scalar production process. Both distributions are expected to peak at the most probable Z^* virtuality, which is

$$m(l_1, l_2) = m(j_1, j_2) = m_A - m_H . \quad (6.4)$$

Due to the very good track momentum resolution, much more precise invariant mass determination is expected in the leptonic channel. Based on the expected performance of the tracking system for ILC and CLIC detectors [55, 56], we estimate the

invariant mass resolution in the leptonic channel to be of the order of 0.1-0.2 GeV, resulting in the statistical precision of the mass difference determination of the order of 10 MeV. As the H boson mass can be known from the charged scalar production analysis, value of $m_A - m_H$ extracted from the invariant mass distributions for the neutral scalar pair production can be used to calculate the value of m_A .

The procedure described above allows for evaluation of all inert scalar masses, i.e. for the full reconstruction of the IDM spectrum. However, there are additional constraints which can be used to test the obtained results, based on the single lepton or single jet energy distribution or the total energy distribution in the neutral scalar pair production events. Energy distribution for single lepton or single jet from the semi-leptonic or fully hadronic decay channel, in the charged scalar pair production, is expected to be flat. However, the maximum allowed energy can be related to scalar masses

$$E_{l/j}^{max} = \frac{E_{beam}}{2}(1 - R) \left(1 + \sqrt{1 - \frac{m_{H^\pm}^2}{E_{beam}^2}} \right). \quad (6.5)$$

Equation (6.5) can be used for independent evaluation of m_{H^\pm} when R value is known. However, determination of the threshold position in the presence of the significant background is an experimental challenge. It requires very good background and detector modeling and We do not consider this measurement in the presented analysis.

The m_A can also be extracted from the neutral scalar pair production events, from energies of leptons or jets coming from Z^* decay. In the laboratory frame the relation between the sum of energies of leptons or jets and neutral scalar masses can be written as:

$$E_{\ell\ell / jj} = \frac{m_A - m_H}{m_A} \sqrt{m_A^2 + \frac{(s - (m_A + m_H)^2)(s - (m_A - m_H)^2)}{4s}} \quad (6.6)$$

However, the value of m_A extracted from this equation turns out to be much more sensitive to the value of m_H than for the method based on the invariant mass measurement.

Following the steps described above, masses of all charged and neutral scalars can be obtained with a statistical precision of the order 100 MeV, as shown in table 21. The systematic shifts observed between the assumed (theo.) scalar masses and the values resulting from the calculations are due to the simplified approach used, but can be corrected based on the simulation results.

7 Conclusions

The Inert Doublet Model was studied as the underlying theoretical framework for light charged and neutral dark scalar production at e^+e^- colliders. For the charged

scalar production, a pair production through $e^+e^- \rightarrow H^+H^-$ was taken as the signal, while for neutral scalars production, $e^+e^- \rightarrow AH$ was considered. Three benchmark scenarios with scalar masses below 200 GeV, obtained recently in [14], were tested and detailed analyses were designed for each considered production channel and final state. Results of the analyses show that, for the considered IDM benchmark scenarios, production of dark scalars should be observable already at the early stages of e^+e^- colliders running at center of mass energy of either 0.5 or 1 TeV. With 500 fb⁻¹ of data, the signal cross section can be measured with precision between 2% and 12%, depending on the considered scenario and decay channel. Using the reconstructed invariant mass and energy distributions of the visible decay products, the masses of dark matter particles can be extracted with a negligible statistical precision, of the order of 100 MeV. Therefore, we expect that precision of the IDM dark scalar mass measurement at the future e^+e^- collider will be dominated by systematic effect.

Acknowledgements

The authors would like to thank Ilya Ginzburg for useful discussions and Tania Robens for useful comments and especially for critical reading of the manuscript. M.H would like to thank Dr. Mogharrab for the operation and maintenance of the computing cluster at Shiraz university. This research was supported by the National Science Centre (Poland) within an OPUS research project 2012/05/B/ST2/03306 (2012-2016).

a) Analysis of $e^+e^- \rightarrow H^+H^- \rightarrow W^+W^-HH$

Channel	Quantity	\sqrt{s} [TeV]	BP1	BP2	BP3
$\ell\nu jjHH$	$m(j_1j_2)$ [GeV]	0.5	58.02 ± 0.10	47.11 ± 0.09	40.48 ± 0.30
		1	59.17 ± 0.11	48.97 ± 0.09	42.32 ± 0.18
$jjjjHH$	$m(j_2j_3)$ [GeV]	0.5	59.68 ± 0.11	49.39 ± 0.12	39.94 ± 0.19
		1	60.90 ± 0.10	50.45 ± 0.08	43.39 ± 0.22
$jjjjHH$	$m(j_1j_4)$ [GeV]	0.5	59.71 ± 0.11	49.64 ± 0.11	40.25 ± 0.18
		1	58.46 ± 0.15	48.48 ± 0.11	43.13 ± 0.21
Average $m_{H^\pm} - m_H$ [GeV]		0.5	59.06 ± 0.06	48.44 ± 0.06	40.16 ± 0.12
		1	59.79 ± 0.07	49.50 ± 0.05	42.86 ± 0.12
$\ell\nu jjHH$	$\sum_{i=1}^2 E(j_i)$ [GeV]	0.5	123.16 ± 0.13	87.33 ± 0.11	58.68 ± 0.40
		1	262.44 ± 0.22	190.95 ± 0.17	130.90 ± 0.31
$jjjjHH$	$\sum_{i=1}^4 E(j_i)$ [GeV]	0.5	248.08 ± 0.17	175.85 ± 0.15	117.99 ± 0.31
		1	525.46 ± 0.27	382.29 ± 0.22	261.85 ± 0.40
Average $R = m_H/m_{H^\pm}$ (in percent)		0.5	50.49 ± 0.03	64.90 ± 0.02	76.42 ± 0.06
		1	47.47 ± 0.02	61.78 ± 0.02	73.82 ± 0.03

b) Analysis of $e^+e^- \rightarrow HA \rightarrow HHZ$

$\ell\ell HH$	$m(\ell_1\ell_2)$ [GeV]	0.5	55.37 ± 0.01	25.37 ± 0.01	5.86 ± 0.07
		1	55.37 ± 0.01	25.37 ± 0.01	5.84 ± 0.03
$jj HH$	$m(j_1j_2)$ [GeV]	0.5	49.21 ± 0.06	20.94 ± 0.03	-
		1	49.58 ± 0.10	21.50 ± 0.05	4.64 ± 0.03
Average $m_A - m_H$ [GeV]		0.5	55.20 ± 0.01	24.93 ± 0.01	5.86 ± 0.07
		1	55.31 ± 0.01	25.22 ± 0.01	5.24 ± 0.02

c) Reconstructed masses

m_{H^\pm} [GeV]	theo.	123	140	176
	0.5	119.29 ± 0.12	138.01 ± 0.17	170.31 ± 0.51
	1	113.82 ± 0.13	129.51 ± 0.13	163.71 ± 0.45
m_H [GeV]	theo.	57.5	85.5	128
	0.5	60.23 ± 0.06	89.57 ± 0.11	130.15 ± 0.39
	1	54.03 ± 0.06	80.01 ± 0.08	120.85 ± 0.33
m_A [GeV]	theo.	113	111	134
	0.5	115.43 ± 0.07	114.50 ± 0.12	136.01 ± 0.46
	1	109.34 ± 0.07	105.23 ± 0.09	126.09 ± 0.36

Table 21: Positions of the reconstructed peaks in the energy and invariant mass distributions for the charged scalar (a) and neutral scalar (b) pair production, and the reconstructed inert scalar masses (c). Different decay channels are considered for center of mass energies of 0.5 and 1 TeV, as indicated in the table. Results on the scalar mass differences, $m_{H^\pm} - m_H$ and $m_A - m_H$, and mass ratio $R = m_H/m_{H^\pm}$ are first averaged over different final states and then used for scalar mass reconstruction as described in the text. Errors indicated correspond to the statistical uncertainties only.

References

- [1] N. G. Deshpande and E. Ma, *Pattern of Symmetry Breaking with Two Higgs Doublets*, *Phys. Rev.* **D18** (1978) 2574.
- [2] Q.-H. Cao, E. Ma, and G. Rajasekaran, *Observing the Dark Scalar Doublet and its Impact on the Standard-Model Higgs Boson at Colliders*, *Phys.Rev.* **D76** (2007) 095011, [[arXiv:0708.2939](#)].
- [3] R. Barbieri, L. J. Hall, and V. S. Rychkov, *Improved naturalness with a heavy Higgs: An Alternative road to LHC physics*, *Phys.Rev.* **D74** (2006) 015007, [[hep-ph/0603188](#)].
- [4] L. Lopez Honorez, E. Nezri, J. F. Oliver, and M. H. G. Tytgat, *The Inert Doublet Model: An Archetype for Dark Matter*, *JCAP* **0702** (2007) 028, [[hep-ph/0612275](#)].
- [5] L. Lopez Honorez and C. E. Yaguna, *The inert doublet model of dark matter revisited*, *JHEP* **1009** (2010) 046, [[arXiv:1003.3125](#)].
- [6] E. M. Dolle and S. Su, *The Inert Dark Matter*, *Phys.Rev.* **D80** (2009) 055012, [[arXiv:0906.1609](#)].
- [7] A. Goudelis, B. Herrmann, and O. Stal, *Dark matter in the Inert Doublet Model after the discovery of a Higgs-like boson at the LHC*, *JHEP* **1309** (2013) 106, [[arXiv:1303.3010](#)].
- [8] M. Krawczyk, D. Sokolowska, P. Swaczyna, and B. Swiezewska, *Constraining Inert Dark Matter by $R_{\gamma\gamma}$ and WMAP data*, *JHEP* **1309** (2013) 055, [[arXiv:1305.6266](#)].
- [9] I. Ginzburg, K. Kanishev, M. Krawczyk, and D. Sokolowska, *Evolution of Universe to the present inert phase*, *Phys.Rev.* **D82** (2010) 123533, [[arXiv:1009.4593](#)].
- [10] T. A. Chowdhury, M. Nemevsek, G. Senjanovic, and Y. Zhang, *Dark Matter as the Trigger of Strong Electroweak Phase Transition*, *JCAP* **1202** (2012) 029, [[arXiv:1110.5334](#)].
- [11] D. Borah and J. M. Cline, *Inert Doublet Dark Matter with Strong Electroweak Phase Transition*, *Phys.Rev.* **D86** (2012) 055001, [[arXiv:1204.4722](#)].
- [12] G. Gil, P. Chankowski, and M. Krawczyk, *Inert Dark Matter and Strong Electroweak Phase Transition*, *Phys.Lett.* **B717** (2012) 396–402, [[arXiv:1207.0084](#)].
- [13] J. M. Cline and K. Kainulainen, *Improved Electroweak Phase Transition with Subdominant Inert Doublet Dark Matter*, *Phys.Rev.* **D87** (2013), no. 7 071701, [[arXiv:1302.2614](#)].
- [14] A. Ilnicka, M. Krawczyk, and T. Robens, *The Inert Doublet Model in the light of LHC and astrophysical data – An Update –*, [[arXiv:1508.01671](#)].
- [15] M. Aoki, S. Kanemura, and H. Yokoya, *Reconstruction of Inert Doublet Scalars at the International Linear Collider*, *Phys. Lett.* **B725** (2013) 302–309, [[arXiv:1303.6191](#)].

- [16] S.-Y. Ho and J. Tandean, *Probing Scotogenic Effects in e^+e^- Colliders*, *Phys. Rev.* **D89** (2014) 114025, [[arXiv:1312.0931](#)].
- [17] E. Lundstrom, M. Gustafsson, and J. Edsjo, *The Inert Doublet Model and LEP II Limits*, *Phys. Rev.* **D79** (2009) 035013, [[arXiv:0810.3924](#)].
- [18] E. Dolle, X. Miao, S. Su, and B. Thomas, *Dilepton Signals in the Inert Doublet Model*, *Phys.Rev.* **D81** (2010) 035003, [[arXiv:0909.3094](#)].
- [19] M. Gustafsson, S. Rydbeck, L. Lopez-Honorez, and E. Lundstrom, *Status of the Inert Doublet Model and the Role of multileptons at the LHC*, *Phys.Rev.* **D86** (2012) 075019, [[arXiv:1206.6316](#)].
- [20] A. Arhrib, Y.-L. S. Tsai, Q. Yuan, and T.-C. Yuan, *An Updated Analysis of Inert Higgs Doublet Model in light of the Recent Results from LUX, PLANCK, AMS-02 and LHC*, *JCAP* **1406** (2014) 030, [[arXiv:1310.0358](#)].
- [21] A. Arhrib, R. Benbrik, and N. Gaur, *$H \rightarrow \gamma\gamma$ in Inert Higgs Doublet Model*, *Phys.Rev.* **D85** (2012) 095021, [[arXiv:1201.2644](#)].
- [22] G. Belanger, B. Dumont, A. Goudelis, B. Herrmann, S. Kraml, and D. Sengupta, *Dilepton constraints in the Inert Doublet Model from Run 1 of the LHC*, *Phys. Rev.* **D91** (2015), no. 11 115011, [[arXiv:1503.07367](#)].
- [23] B. Swiezewska and M. Krawczyk, *Diphoton rate in the inert doublet model with a 125 GeV Higgs boson*, *Phys.Rev.* **D88** (2013), no. 3 035019, [[arXiv:1212.4100](#)].
- [24] I. F. Ginzburg, *Measuring mass and spin of Dark Matter particles with the aid energy spectra of single lepton and dijet at the e^+e^- Linear Collider*, *J. Mod. Phys.* **5** (2014) 1036–1049, [[arXiv:1410.0869](#)].
- [25] T. Barklow, J. Brau, K. Fujii, J. Gao, J. List, N. Walker, and K. Yokoya, *ILC Operating Scenarios*, [arXiv:1506.07830](#).
- [26] N. Blinov, J. Kozaczuk, D. E. Morrissey, and A. de la Puente, *Compressing the Inert Doublet Model*, [arXiv:1510.08069](#).
- [27] B. Świeżewska, *Yukawa independent constraints for two-Higgs-doublet models with a 125 GeV Higgs boson*, *Phys. Rev.* **D88** (2013), no. 5 055027, [[arXiv:1209.5725](#)].
[Erratum: *Phys. Rev.* **D88**, no. 11, 119903 (2013)].
- [28] B. Swiezewska, *Inert scalars and vacuum metastability around the electroweak scale*, *JHEP* **07** (2015) 118, [[arXiv:1503.07078](#)].
- [29] P. M. Ferreira and B. Swiezewska, *One-loop contributions to neutral minima in the inert doublet model*, [arXiv:1511.02879](#).
- [30] **ATLAS, CMS** Collaboration, G. Aad et al., *Combined Measurement of the Higgs Boson Mass in pp Collisions at $\sqrt{s} = 7$ and 8 TeV with the ATLAS and CMS Experiments*, *Phys. Rev. Lett.* **114** (2015) 191803, [[arXiv:1503.07589](#)].
- [31] **CMS** Collaboration, V. Khachatryan et al., *Constraints on the Higgs boson width*

- from off-shell production and decay to Z -boson pairs, *Phys. Lett.* **B736** (2014) 64, [[arXiv:1405.3455](#)].
- [32] **ATLAS** Collaboration, G. Aad et al., *Constraints on the off-shell Higgs boson signal strength in the high-mass ZZ and WW final states with the ATLAS detector*, *Eur. Phys. J.* **C75** (2015), no. 7 335, [[arXiv:1503.01060](#)].
- [33] **Particle Data Group** Collaboration, K. A. Olive et al., *Review of Particle Physics*, *Chin. Phys.* **C38** (2014) 090001.
- [34] **LUX** Collaboration, D. S. Akerib et al., *First results from the LUX dark matter experiment at the Sanford Underground Research Facility*, *Phys. Rev. Lett.* **112** (2014) 091303, [[arXiv:1310.8214](#)].
- [35] A. Pierce and J. Thaler, *Natural Dark Matter from an Unnatural Higgs Boson and New Colored Particles at the TeV Scale*, *JHEP* **08** (2007) 026, [[hep-ph/0703056](#)].
- [36] G. Altarelli and R. Barbieri, *Vacuum polarization effects of new physics on electroweak processes*, *Phys. Lett.* **B253** (1991) 161–167.
- [37] M. E. Peskin and T. Takeuchi, *A New constraint on a strongly interacting Higgs sector*, *Phys. Rev. Lett.* **65** (1990) 964–967.
- [38] I. Maksymyk, C. P. Burgess, and D. London, *Beyond S , T and U* , *Phys. Rev.* **D50** (1994) 529–535, [[hep-ph/9306267](#)].
- [39] M. E. Peskin and T. Takeuchi, *Estimation of oblique electroweak corrections*, *Phys. Rev.* **D46** (1992) 381–409.
- [40] **Planck** Collaboration, P. A. R. Ade et al., *Planck 2015 results. XIII. Cosmological parameters*, [[arXiv:1502.01589](#)].
- [41] **CompHEP** Collaboration, E. Boos, V. Bunichev, M. Dubinin, L. Dudko, V. Ilyin, A. Kryukov, V. Edneral, V. Savrin, A. Semenov, and A. Sherstnev, *CompHEP 4.4: Automatic computations from Lagrangians to events*, *Nucl. Instrum. Meth.* **A534** (2004) 250–259, [[hep-ph/0403113](#)].
- [42] A. Pukhov, E. Boos, M. Dubinin, V. Edneral, V. Ilyin, D. Kovalenko, A. Kryukov, V. Savrin, S. Shichanin, and A. Semenov, *CompHEP: A Package for evaluation of Feynman diagrams and integration over multiparticle phase space*, [[hep-ph/9908288](#)].
- [43] A. Semenov, *LanHEP: A package for automatic generation of Feynman rules from the Lagrangian*, *Comput. Phys. Commun.* **115** (1998) 124–139.
- [44] A. V. Semenov, *Automatic generation of Feynman rules from the Lagrangian by means of LanHEP package*, *Nucl. Instrum. Meth.* **A389** (1997) 293–294.
- [45] T. Sjostrand, S. Mrenna, and P. Z. Skands, *A Brief Introduction to PYTHIA 8.1*, *Comput. Phys. Commun.* **178** (2008) 852–867, [[arXiv:0710.3820](#)].
- [46] T. Ohl, *CIRCE version 1.0: Beam spectra for simulating linear collider physics*, *Comput. Phys. Commun.* **101** (1997) 269–288, [[hep-ph/9607454](#)].

- [47] M. Cacciari, *FastJet: A Code for fast k_t clustering, and more*, in *Deep inelastic scattering. Proceedings, 14th International Workshop, DIS 2006, Tsukuba, Japan, April 20-24, 2006*, pp. 487–490, 2006. [hep-ph/0607071](#). [,125(2006)].
- [48] M. Cacciari, G. P. Salam, and G. Soyez, *FastJet User Manual*, *Eur. Phys. J.* **C72** (2012) 1896, [[arXiv:1111.6097](#)].
- [49] A. F. Żarnecki, “Sensitivity to top FCNC decay $t \rightarrow ch$ at future e^+e^- colliders.” presented at Workshop on Top Physics at Lepton Colliders, Valencia, Spain, June 30 – July 3, 2015.
- [50] M. A. Thomson, *Particle Flow Calorimetry and the PandoraPFA Algorithm*, *Nucl. Instrum. Meth.* **A611** (2009) 25–40, [[arXiv:0907.3577](#)].
- [51] R. Brun and F. Rademakers, *ROOT: An object oriented data analysis framework*, *Nucl. Instrum. Meth.* **A389** (1997) 81–86.
- [52] **Particle Data Group** Collaboration, K. A. Olive et al., *Review of Particle Physics*, *Chin. Phys.* **C38** (2014) 090001.
- [53] D. Eriksson, J. Rathsmann, and O. Stal, *2HDMC: Two-Higgs-Doublet Model Calculator Physics and Manual*, *Comput. Phys. Commun.* **181** (2010) 189–205, [[arXiv:0902.0851](#)].
- [54] D. Eriksson, J. Rathsmann, and O. Stal, *2HDMC: Two-Higgs-doublet model calculator*, *Comput. Phys. Commun.* **181** (2010) 833–834.
- [55] H. Abramowicz et al., *The International Linear Collider Technical Design Report - Volume 4: Detectors*, [arXiv:1306.6329](#).
- [56] M. Aicheler, M. Aicheler, P. Burrows, M. Draper, T. Garvey, P. Lebrun, K. Peach, N. Phinney, H. Schmickler, D. Schulte, et al., *A Multi-TeV Linear Collider Based on CLIC Technology*, .